

Detection of Blob Objects in Microscopic Zebrafish Images Based on Gradient Vector Diffusion

Gang Li,^{1,2} Tianming Liu,^{2,3} Jingxin Nie,^{1,2} Lei Guo,¹ Jarema Malicki,⁴ Andrew Mara,⁵ Scott A. Holley,⁵ Weiming Xia,^{6,7} Stephen T. C. Wong^{2,3*}

¹School of Automation, Northwestern Polytechnic University, Xi'an, China

²Center for Bioinformatics, Harvard Center for Neurodegeneration and Repair, Harvard Medical School, Boston, Massachusetts

³Functional and Molecular Imaging Center, Department of Radiology, Brigham and Women's Hospital, Boston, Massachusetts

⁴Department of Ophthalmology, Harvard Medical School, Boston, Massachusetts

⁵Department of Molecular, Cellular and Developmental Biology, Yale University, New Haven, Connecticut

⁶Center for Neurologic Disease, Brigham and Women's Hospital, Harvard Medical School, Boston, Massachusetts

⁷Department of Neurology, Brigham and Women's Hospital, Harvard Medical School, Boston, Massachusetts

*Correspondence to: Stephen Wong, Center for Bioinformatics, Harvard Center for Neurodegeneration and Repair, Harvard Medical School, 1249 Boylston Street, 346, Boston, MA 02215, USA.

Email: wong@crystal.harvard.edu

Published online 25 July 2007 in Wiley InterScience (www.interscience.wiley.com)

DOI: 10.1002/cyto.a.20436

• Abstract

The zebrafish has become an important vertebrate animal model for the study of developmental biology, functional genomics, and disease mechanisms. It is also being used for drug discovery. Computerized detection of blob objects has been one of the important tasks in quantitative phenotyping of zebrafish. We present a new automated method that is able to detect blob objects, such as nuclei or cells in microscopic zebrafish images. This method is composed of three key steps. The first step is to produce a diffused gradient vector field by a physical elastic deformable model. In the second step, the flux image is computed on the diffused gradient vector field. The third step performs thresholding and nonmaximum suppression based on the flux image. We report the validation and experimental results of this method using zebrafish image datasets from three independent research labs. Both sensitivity and specificity of this method are over 90%. This method is able to differentiate closely juxtaposed or connected blob objects, with high sensitivity and specificity in different situations. It is characterized by a good, consistent performance in blob object detection. © 2007 International Society for Analytical Cytology

• Key terms

zebrafish; image-based phenotyping; blob object detection; Alzheimer's disease; retina; somitogenesis; image analysis; elastic deformable model; gradient vector diffusion

THE zebrafish (*Danio rerio*) has become an invaluable vertebrate model system for developmental biology studies, functional genomics, disease modeling, and drug discovery (1–12). Female zebrafish produce large clutches of externally developing, transparent embryos that complete gastrulation, neurulation, and much of organogenesis within the first 24 h of development. These features form the basis for one of the great strengths of the zebrafish as a model system: the ability to visualize early developmental events in the living embryo and to use digital microscopic imaging to phenotype zebrafish in vivo. However, the tremendous variety of digital images generated from large numbers of embryos frequently leads to a bottleneck in data analysis and interpretation. While computerized analysis of biological images has been extensively explored, e.g., quantitative analysis of cells (13) and morphological analysis of neurons (14), few studies have been reported for automated zebrafish image quantification.

The quantification of blob objects in microscopic zebrafish images has become a common task in quantitative phenotypic analysis of zebrafish, and usually involves a comparison of the number of cells (15) or subcellular structures (16) between normal and mutant or compound-treated zebrafish. The types of blob objects in zebrafish images are diverse. In this study, we use nuclei, cells and neurons to exemplify blob objects. The common property of blob objects is that they are connected regions of interest with extent both in space and in grey-level. Generally, a blob object consists of one extremum and one saddle point. Its mathematical definition has been provided previously (17).

Received 30 June 2006; Revision Received 30 April 2007;
Accepted 31 May 2007

© 2007 International Society for Analytical Cytology

Grant sponsor: Harvard Center for Neurodegeneration and Repair
(Bioinformatics Research Center Program Grant), Harvard Medical
School (SW)

In recent years, successful efforts have been made to develop image analysis methods for automated blob object detection (18–25). For example, Sjostrom et al. (18) used the artificial neural network for automatic cell counting. Chen et al. (19) developed a cellular image analysis method to segment, classify and track individual cells in a living cell population. Shain et al. (20) developed a method for 3D counting of cell nuclei. Lin et al. (21) proposed an improved watershed method for nuclei segmentation in confocal image stacks. Yang and Parvin (22) detected blob objects by analyzing Hessian matrices. They also proposed a method based on iterative voting along the gradient direction to determine the centers of blobs (23). Byun et al. (24) utilized the inverted Laplacian of Gaussian for blob detector in the application of detecting nuclei in immunofluorescent retinal images.

Unique screening applications in zebrafish have motivated us to develop a new method for blob object quantification. The first major challenge in the quantification of blob objects in microscopic zebrafish images is that frequently there are many blobs touching each other or connecting together (see, for example, the images of nuclei in Fig. 3). The ability to differentiate such touching or connected blob objects is the first goal of the proposed method. The second goal is to provide a general and robust approach to deal with quite different blob images generated from zebrafish labs that address diverse biological problems (in this work, we use images from three labs that focus on different organs). As a result, this method should be broadly useful to many labs in the zebrafish research community.

MATERIALS AND METHODS

Zebrafish Images

We report the validation of this algorithm and experimental results using microscopic zebrafish image datasets from three zebrafish research labs (Malicki Lab of Harvard Medical School, Holley Lab of Yale University, and Xia Lab of Harvard Medical School). The zebrafish retina images from the Malicki lab were acquired using a Leica SP2 confocal microscope from transverse cryosections stained with DNA-binding dye Yo-Pro (3,5). Cryosections were collected on glass slides, coverslipped, and analyzed using a 40 \times oil immersion lens. The zebrafish images from the Holley lab are confocal sections of presomitic mesoderm nuclei using high-resolution fluorescent in situ hybridization (7,8). The zebrafish images from the Xia lab are Rohon–Beard (RB) sensory neurons in the spinal cord stained with anti-acetylated tubulin antibody (26).

Method Overview

The proposed method is composed of three key steps, as shown in Figure 1. The central idea of our method (the first step in Fig. 1) is to use the diffused gradient vector field, in which each point flows toward (or outward from) a sink, to detect the blob object. The diffused gradient vector field is obtained by a physical elastic deformable model. In the second step, we compute the flux image on the diffused gradient vector field. This step is followed by thresholding and nonmaximum suppression in the third step, generating a series of centers of blobs in the result image. The major advantage of this method is its robustness and applicability to many situations, which we demonstrate in the Results section. The limitation is that it is based on the assumption that the central areas of the blob objects are brighter or darker than peripheral areas. This condition guides the gradient diffusion toward or far away from the centers of blob objects, even though the blob objects may closely touch each other. For other conditions, such as textured blob objects, the gradient vector field would be cluttered and the detection results would be wrong.

Gradient Vector Diffusion Using Elastic Deformable Model

The image gradient provides important information for image analysis tasks. For example, the gradient vectors point to the central areas if the central areas are brighter than peripheral areas, or point away from the central areas if the central areas are darker. This information can be exploited to guide the detection of blobs. In practice, however, the gradient magnitude becomes very small, and the direction of gradient vector is usually untrustworthy due to the noise in the image, when approaching the central areas of blobs. Therefore, we utilize a

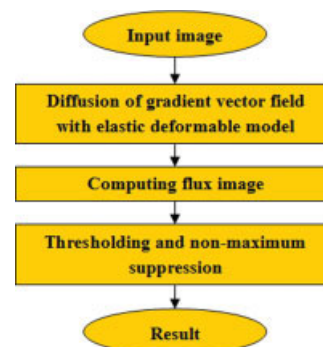


Figure 1. Flowchart of the proposed method. [Color figure can be viewed in the online issue, which is available at www.interscience.wiley.com.]

physical model to diffuse the gradient vectors on the image boundaries throughout the image. This gradient vector diffusion, which can propagate gradient vectors with large magnitude to the areas with weak gradient vectors and can smooth the noisy gradient vector field, has been widely used in the image processing field (27). In this study, we adopt an elastic deformable model, under which the image is modeled as elastic sheets warped by an external force field to achieve gradient vector diffusion. This model has been introduced in (28,29) for medical image registration, where the deformation of boundary points are fixed, and then the deformation field is propagated to the inner region of an image by solving the elastic model equation.

The diffusion gradient vector field $\mathbf{v}(x, y) = (u(x, y), v(x, y))$ in a 2D image is defined to be a solution to the partial differential equation (PDE) describing the deformation of an elastic sheet (28):

$$\mu \nabla^2 \mathbf{v} + (\lambda + \mu) \nabla \text{div}(\mathbf{v}) + q(\nabla f - \mathbf{v}) = 0 \quad (1)$$

where ∇^2 is the Laplacian operator, div is the divergence operator, ∇ is the gradient operator, and μ and λ are the Lamé elastic material constants. In this study, we aim to diffuse the gradient vectors to the central areas of blob objects. Therefore, f is set to be

$$\begin{aligned} f_1(x, y) &= G_\sigma(x, y) * I(x, y) \\ f_2(x, y) &= -G_\sigma(x, y) * I(x, y) \end{aligned}$$

where $I(x, y)$ is a gray-level image and $G_\sigma(x, y)$ is a two-dimensional Gaussian function with standard derivation σ . Note that f_1 is designed for detection of bright blobs, whereas f_2 is designed for detection of dark blobs. q is a function indicating whether or not the displacement is prefixed at the position. In our method, the indicator function is set as

$$q(x, y) = \begin{cases} 1 & |\nabla f(x, y)| > 0 \\ 0 & \text{otherwise} \end{cases}$$

The model is solved by treating u and v as functions of time:

$$\begin{cases} \mathbf{v}_t(x, y, t) = \mu \nabla^2 \mathbf{v}(x, y, t) + (\lambda + \mu) \nabla \text{div}(\mathbf{v}(x, y, t)) \\ \quad + q(x, y)(\nabla f(x, y) - \mathbf{v}(x, y, t)) \\ \mathbf{v}(x, y, 0) = \nabla f(x, y) \end{cases} \quad (2)$$

where $\mathbf{v}_t(x, y, t)$ denotes the partial derivative of $\mathbf{v}(x, y, t)$ with respect to time t . The equation is decoupled as

$$\begin{aligned} u_t(x, y, t) &= \mu \nabla^2 u(x, y, t) + (\lambda + \mu)(\nabla \text{div}(\mathbf{v}(x, y, t)))_x \\ &\quad + q(x, y)((\nabla f(x, y))_x - u(x, y, t)) \\ v_t(x, y, t) &= \mu \nabla^2 v(x, y, t) + (\lambda + \mu)(\nabla \text{div}(\mathbf{v}(x, y, t)))_y \\ &\quad + q(x, y)((\nabla f(x, y))_y - v(x, y, t)) \end{aligned}$$

In our numerical implementation, the spacing interval Δx and Δy , and time interval Δt are all set to be 1. The indices i, j , and n correspond to x, y , and t , respectively. Then the equations are approximated as:

$$\begin{aligned} u_t &= u_{i,j}^{n+1} - u_{i,j}^n, \nabla^2 u = u_{i+1,j} + u_{i-1,j} + u_{i,j+1} + u_{i,j-1} - 4u_{i,j} \\ v_t &= v_{i,j}^{n+1} - v_{i,j}^n, \nabla^2 v = v_{i+1,j} + v_{i-1,j} + v_{i,j+1} + v_{i,j-1} - 4v_{i,j} \\ (\nabla \text{div}(\mathbf{v}))_x &= u_{i+1,j} + u_{i-1,j} - 2u_{i,j} + v_{i+1,j+1} - v_{i,j+1} - v_{i+1,j-1} + v_{i,j-1} \\ (\nabla \text{div}(\mathbf{v}))_y &= v_{i+1,j} + v_{i-1,j} - 2v_{i,j} + u_{i+1,j+1} - u_{i,j+1} - u_{i+1,j-1} + u_{i,j-1} \\ (\nabla f)_x &= f_{i+1,j} - f_{i,j}, (\nabla f)_y = f_{i,j+1} - f_{i,j} \end{aligned}$$

The solution to Eq. (2) defines the displacement of each position in an elastic object, when displacements at some locations are prefixed. Consider \mathbf{v} in Eq. (2) as a velocity rather than a displacement field, according to hydromechanics, the second term in Eq. (2) denotes the compression of a compressible fluid, and $\text{div}(\mathbf{v}) = 0$ indicates an incompressible fluid. The μ and λ in Eq. (2) determine the tradeoff between conformability to the prefixed deformation vectors and smoothness of the deformation field (28). When μ and λ are small, the prefixed deformation vectors are well preserved, whereas if μ and λ are large, the obtained deformation field is smoother. Figure 2 shows a zoomed normalized diffused gradient vector field using the elastic deformable model compared with the original gradient vector field. Obviously, the diffused gradient vector field using the elastic deformable model smoothly flows toward the central areas of blobs. The red arrows in Figure 2 highlight examples, in which the diffused gradient vectors in a blob converge to a central point,

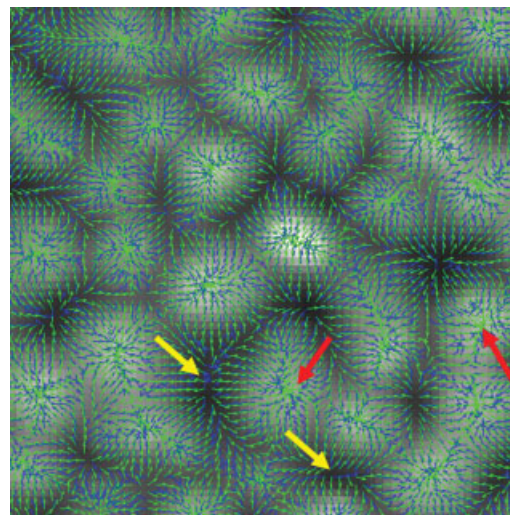


Figure 2. Normalized diffused gradient vector field (green arrows) and the original gradient vector field (blue arrows) overlaid on the original intensity image cropped from a 2D image of zebrafish nuclei. The diffused gradient vector field smoothly flows toward the central areas of blobs. The red arrows highlight examples, in which the diffused gradient vectors in a blob converge to a central point, while the original gradient vectors do not converge. Moreover, even though blob objects are closely juxtaposed, the diffused gradient vectors split along a clear boundary and flow towards the corresponding central areas of each blob. The yellow arrows show examples where the diffused gradient vectors have better boundaries than the original gradients. [Color figure can be viewed in the online issue, which is available at www.interscience.wiley.com.]

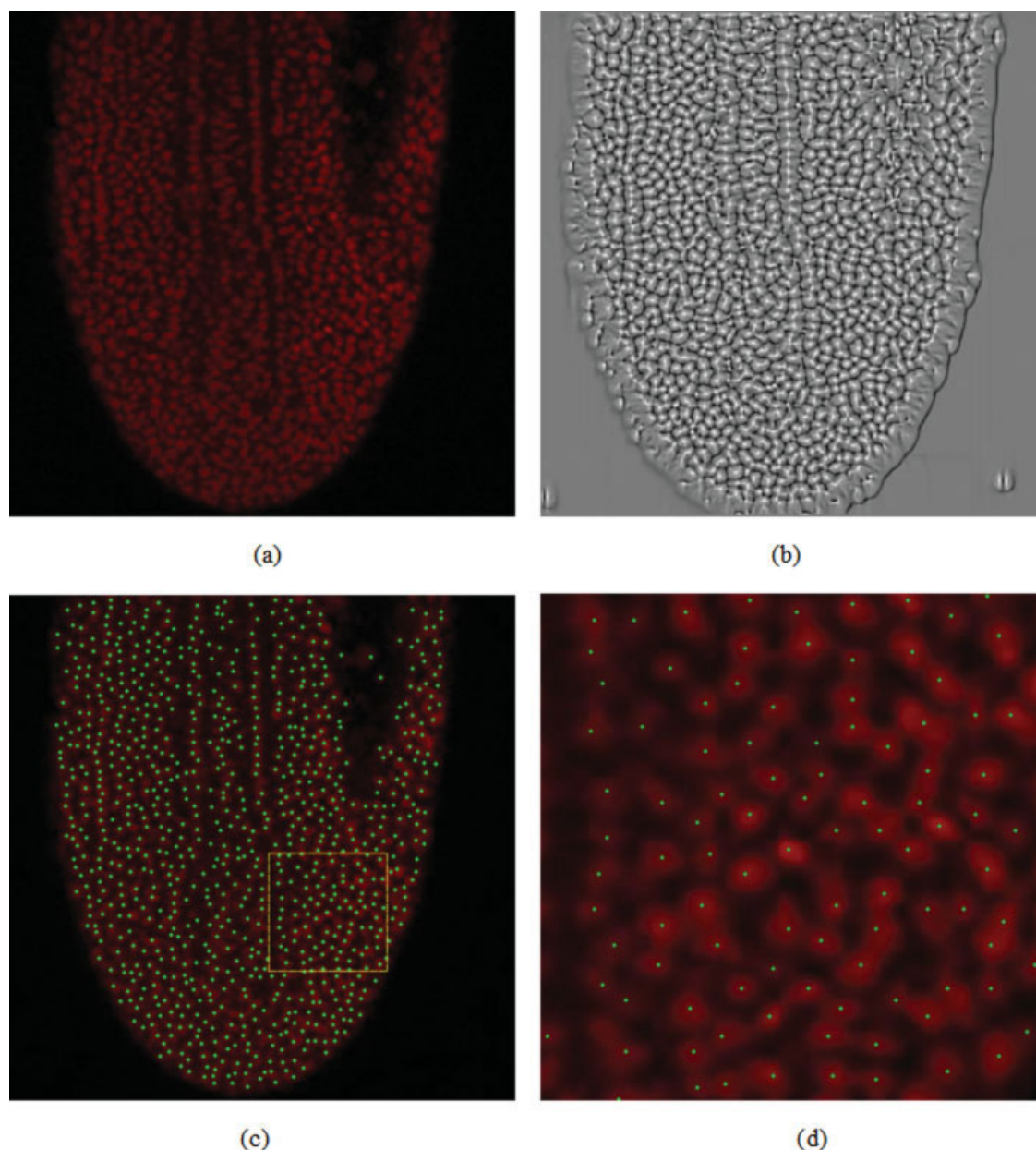


Figure 3. Illustration of the blob detection procedure. (a) Input zebrafish presomitic mesoderm image. (b) The flux image computed from diffused gradient vector field with elastic deformable model. Here, the flux image is reversed, and bright color indicates negative flux. (c) The blob center detection result, revealing 885 nuclei in total, overlaid on the original color image. The green dots represent the centers of detected nuclei (d) An enlargement of the region enclosed within the yellow box in (c). [Color figure can be viewed in the online issue, which is available at www.interscience.wiley.com.]

while the original gradient vectors do not converge. Moreover, even though blob objects are closely juxtaposed, the diffused gradient vectors split along a clear boundary and flow towards the corresponding central areas of each blob. This property greatly contributes to the achievement of the first goal as described in the Introduction section, which will be extensively validated in the Results section. The yellow arrows in Figure 2 show examples where the diffused gradient vectors have better boundaries than the original gradients.

Divergence and Flux

On the basis of the diffused gradient vectors, we compute the flux of the diffused gradient vector field, which is analogous to the flow of an incompressible fluid. In physical terms, the divergence of a vector field is the extent to which the vector field behaves like a source or a sink at a given point. The divergence of a vector field $\mathbf{F} = (F_x(x,y), F_y(x,y))$ at a point is defined as net outward flux per unit volume V , in the limit $V \rightarrow 0$ (30):

$$\text{div}(\mathbf{F}) \equiv \lim_{V \rightarrow 0} \frac{\int_S \langle \mathbf{F}, \mathbf{N} \rangle ds}{V}$$

where V is the volume, S is the closed surface, and \mathbf{N} is the outward normal at each point on the closed surface. This formula for the divergence of a vector field can be written in Cartesian coordinates as the sum of partial derivatives with respect to each of vector field component directions:

$$\text{div}(\mathbf{F}) = \frac{\partial F_x}{\partial x} + \frac{\partial F_y}{\partial y}$$

If the divergence at a point is positive, then it is called a source. Otherwise, it is called a sink. As mentioned in the Gradient Vector Diffusion Using Elastic Deformable Model section, we set the diffused gradient flow as directed towards the blob center, regardless of whether the central area of a blob object is brighter or darker than peripheral points. Thus, we only deal with the detection of sinks.

However, the points that we are interested in are not all differentiable, as Eq. (2) cannot be used at these points when the vector field is singular (30). According to divergence theorem, also known as Gauss's theorem, we have

$$\int_V \text{div}(\mathbf{F}) dV = \int_S \langle \mathbf{F}, \mathbf{N} \rangle ds$$

This equation means that the net outward flux through the surface, which bounds a finite volume equals the volume integral of the divergence of the vector field within the volume. In the numerical implementation, the flux at point $\mathbf{x} = (x, y)$ is computed as:

$$\text{Flux}(\mathbf{x}) = \sum_{i=1}^8 \langle \mathbf{N}_i, \mathbf{F}(\mathbf{x}_i) \rangle$$

where \mathbf{x}_i is a 8-neighbor of \mathbf{x} , and \mathbf{N}_i is the outward normal at \mathbf{x}_i on the unit circle centered at \mathbf{x} . It is noted that before computing the flux image, the diffused gradient vector is normalized.

Thresholding and Nonmaximum Suppression

As we can see in the previous section, the centers of blob objects correspond to the sinks of the diffused gradient vector field, where the flux are local minima. To detect blob centers, nonmaximum suppression is applied to the reversed flux image. A threshold T is applied to the reversed flux image to determine the candidate centers of the blobs. Then, a distance R that approximates the average radius of the blobs in the image is used as the search range to look for local maximums on candidate points. After these thresholding and nonmaximum suppression steps, the final detection result is obtained. Figure 3 shows a run-through example of the blob detection.

Parameter Selection

Two key parameters in the proposed method for blob object detection will be discussed in turn.

The threshold T . As mentioned in the Thresholding and Nonmaximum Suppression section, the threshold parameter T is used to determine the candidate centers of the blobs from the reversed flux image. If a pixel intensity in the reversed flux image is larger than T , it is selected as a center candidate. In the theoretical limit, the reversed flux at the center of a blob is 8. However, because of the digital error and noise in the image, it cannot reach the theoretical limit. In practice, the threshold T is always set to be < 8 . The larger the threshold T is, the less candidate points are found. Using the image in Figure 3a as an example, we set a series of T values from 1.0 to 7.0 with an interval of 0.5 to evaluate the number of nuclei detected. We set the search range at $R = 5$, which is the approximate average radius of nuclei in this image. Using these settings, the numbers of nuclei detected range from 970 ($T = 1.0$) to 780 ($T = 7.0$), as shown in Figure 4a. In particular, when T changes from 1.0 to 6.0, there is no significant difference in the numbers of detected nuclei, and the detection error percentage is consistently less than 9.8%. This result demonstrates that the proposed method is not very sensitive to the selection of the parameter T . This property renders the generalizability of this method to different blob images generated from zebrafish labs that address diverse biological problems, which is part of the second goal as described in Section 1. In the experiments described in the Results section, we

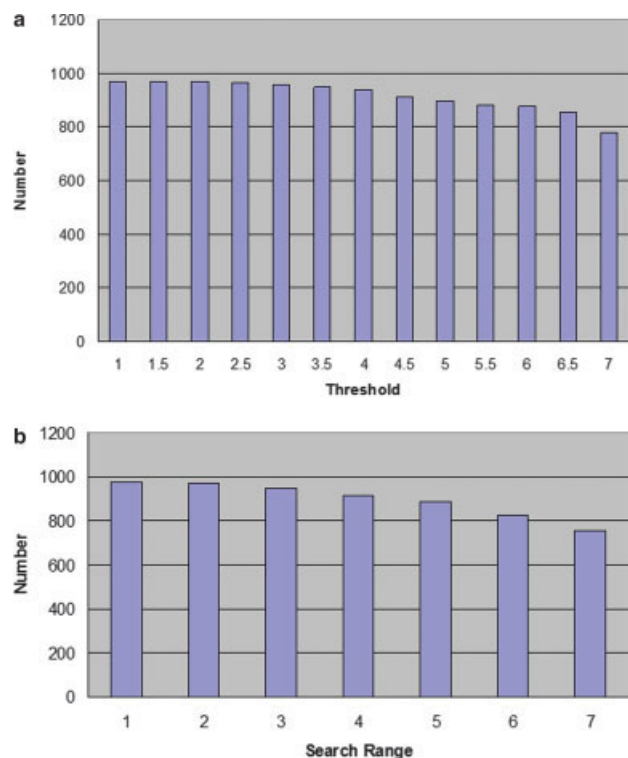


Figure 4. (a) The blob detection result varies with the threshold parameter T . (b) The blob detection result varies with the search radius R . Those figures are related to the image in Figure 3a. [Color figure can be viewed in the online issue, which is available at www.interscience.wiley.com.]

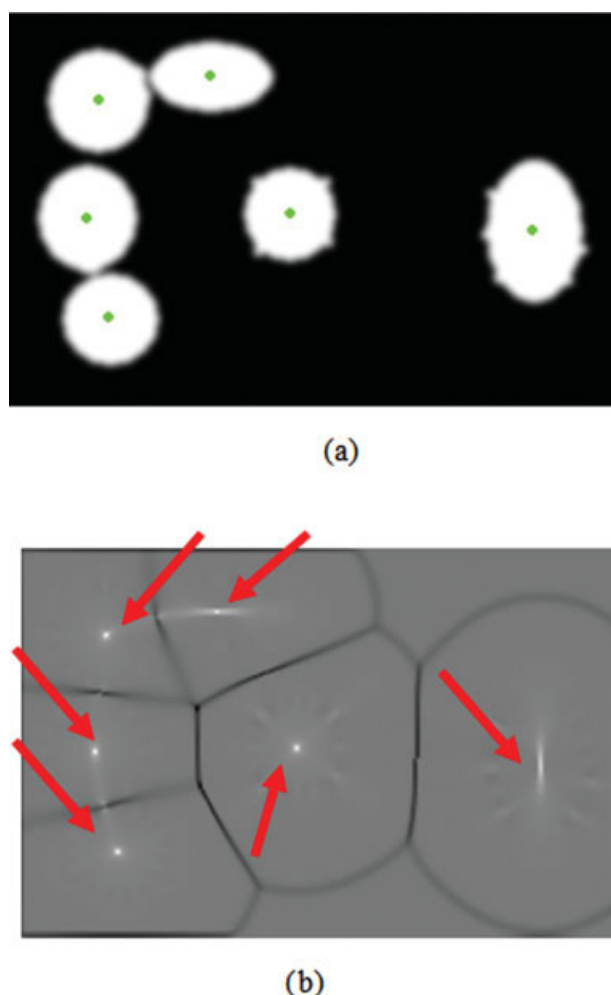


Figure 5. A synthesized image containing discs and ellipses is used to illustrate that the method is not sensitive to the shapes of blob objects. (a) The detected centers (green points) of blobs overlaid on the original image. (b) The flux image where the bright color indicates that the flux is negative and the dark color indicates that the flux is positive. The red arrows point to the sinks. [Color figure can be viewed in the online issue, which is available at www.interscience.wiley.com.]

chose the threshold T as 5.5. When T is set to be larger than 6.0, which approaches the theoretical limit, more centers of nuclei are missed due to the noise and digital error.

The search radius R . The search radius R is used to find the local maxima in the reversed flux image. If the threshold R is set too large, few candidate centers of blobs will be found. If R is set too small, many false centers of blobs will be found. An appropriate choice is to set R close to the average radius of blobs in the image. In this experiment, we use a series of R values ranging from 1.0 to 7.0 with an interval of 1 to evaluate the nuclei detection result, using the image in Figure 3a. Using these settings, the numbers of nuclei detected range from 973 ($R = 1$) to 756 ($R = 7$), as shown in Figure 4b. The average radius of nuclei in the image is ~ 5 pixels. When R varies from

1 to 5, the number of detected points changes from 973 to 885, with the error percentage consistently $< 9.04\%$. However, when R is set larger than 5, the number of detected blobs decreases rapidly, as shown in Figure 4b. This result indicates that the method is not sensitive when the search radius R is relatively small. This property greatly helps to achieve the second goal outlined in the Introduction. While using this method, selection of relatively large R values should be avoided.

RESULTS

Validation on Synthesized Images

In this section, a series of synthesized blob images are used as ground-truth to validate the method. At the same time, we evaluate the robustness of this method in situations in which there are various shapes of blobs, different sizes of the blobs, and a range of noise and lighting conditions. In all of the experiments below, the parameters are fixed at: $R = 5$ and $T = 5.5$.

Applicability to various shapes. To examine the applicability of this method to various shapes of blobs in the same image, we synthesized an image containing several discs and ellipses that touch each other, as shown in Figure 5a. The proposed method found all of the centers of the blobs (green dots in Fig. 5a), even though the shapes of the blobs are quite different. Figure 5b shows the reversed flux image. This experimental result demonstrates that this method is applicable to different shapes of blob objects. This robustness originates from the fact that diffused gradient vectors tend to converge to a central point, as represented by white dots (which are also highlighted by the arrows) in Figure 5b.

Applicability to different sizes. We generated an image containing disks and ellipses of different sizes touching each other, as shown in Figure 6a. Although the sizes and shapes of these blobs vary significantly, the proposed method is able to detect all of the centers of the blobs correctly, as represented by the green dots in Figure 6a. The result indicates that the proposed method is applicable to different sizes of blob objects, given

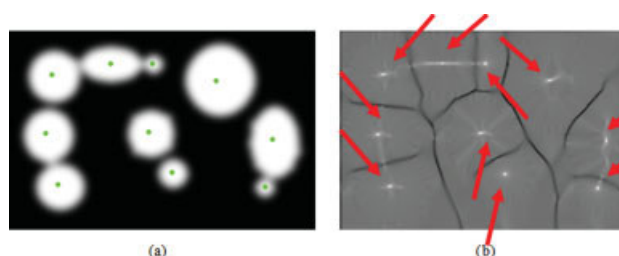


Figure 6. A synthesized image containing discs and ellipses with different sizes is used to illustrate that the method is not sensitive to the sizes of blob objects. (a) The detected centers (green points) of blobs overlaid on the original image. (b) The flux image where the bright color indicates that the flux is negative and the dark color indicates that the flux is positive. The red arrows point to the sinks. [Color figure can be viewed in the online issue, which is available at www.interscience.wiley.com.]

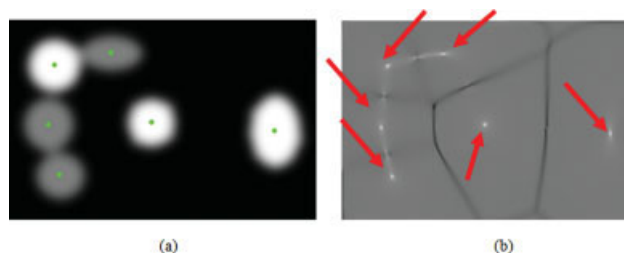


Figure 7. A synthesized image containing discs and ellipses of different brightness is used to illustrate that the method is not sensitive to the brightness of blob objects. (a) The detected centers (green points) of blobs are overlaid on the original image. (b) The flux image where the bright color indicates that the flux is negative and the dark color indicates that the flux is positive. The red arrows point to the sinks. [Color figure can be viewed in the online issue, which is available at www.interscience.wiley.com.]

that the same parameters are applied. Figure 6b shows the reversed flux image and the converged central points are highlighted by the red arrows. The results presented here further support the proposition in the Parameter Selection section that the proposed method is quite insensitive to selection of parameters and is applicable to the analysis of different blob sizes in the same image.

Applicability to different lighting conditions. As lighting conditions have little effect on the flux image computed from the normalized gradient vector field using the elastic deformable model (Gradient Vector Diffusion Using Elastic Deformable Model section), the proposed method is expected to be applicable to different lighting conditions. To demonstrate this, we used a simulated image containing discs and ellipses of different intensities, as shown in Figure 7a. The detected centers of blobs, represented by the green dots in Figure 7a, show that all of the blobs are detected correctly. Figure 7b shows the reversed flux image and the converged central points are highlighted by the red arrows. This result supports the conclusion that the proposed method is insensitive to different lighting conditions.

Robustness to the noise. Many types of noise are present in microscopic images of zebrafish acquired via light microscopy. Therefore, any method for blob detection should be as insensitive to noise in the image as possible. To examine whether the proposed method can tolerate noise, we synthesized an image containing discs and ellipses that touch each other. Then, we added Gaussian noise to the image, as shown in Figure 8a. The blob detection results are overlaid on the original blobs as shown in the Figure 8a. It is evident that all blobs are detected correctly. Figure 8b shows the reversed flux image and the converged central points are highlighted by the red arrows. These results support the conclusion that the proposed method tolerates high noise levels. This robustness comes from the strong tendency of the diffused gradient vectors to converge to a central point within a blob.

Validation on Real Microscopic Zebrafish Images

The proposed method has been applied to microscopic zebrafish images from three independent research labs in order to test its utility and versatility. The experimental data and their analysis are discussed below. We emphasize that this study focuses on the evaluation of the algorithm and that the biological questions represented by these datasets are addressed in other publications.

Presomitic mesoderm nuclei detection. Zebrafish somite segmentation is governed by a clock that generates oscillations in gene expression in the field of cells to be segmented, called the presomitic mesoderm (7,8). Different phases within the oscillation can be identified by the subcellular localization of oscillating mRNA in each cell (31). A first step to automating the classification of the phase of each cell is to accurately identify each cell nucleus within the presomitic mesoderm.

We applied the proposed method to identify and quantify cell nuclei in the zebrafish presomitic mesoderm. Figure 9 shows two examples of the nuclei detection result. The dataset is provided by the Holley Lab at Yale University. The automatically detected nuclei are represented by green dots overlaid on the original image, as shown in Figure 9a. It is evident that most of the nuclei are correctly detected. To evaluate the performance of this method, we compared the automated result to expert manual labeling, as shown in Figure 9a. To quantify this comparison we use false negative rates and false positive rates. A false negative is a nucleus that is not detected, while a false positive is an object that is not a cell nucleus, but is detected as a cell nucleus by the method. In the case of this study, the false negative and positive rates are 1.1 and 0.2%, respectively, compared with expert manual labeling (Case 1 in Table 1). Figure 9b shows another example of nuclei detection. For the second example, the false negative rate and false positive rate are 2.6 and 0.3%, compared with expert manual counting (Case 2 in Table 1).

The proposed method has been applied to 10 images of zebrafish presomitic mesoderm nuclei. The average false negative and false positive rates are 2.0 and 0.2%, respectively. The

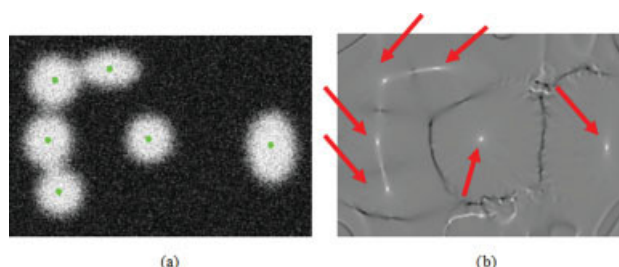


Figure 8. A synthesized image containing circles and ellipses blurred by an addition of Gaussian noise is used to illustrate that the method is not sensitive to noise. (a) The detected centers (green points) of blobs overlaid on the original image. (b) The flux image where the bright color indicates that the flux is negative and the dark color indicates that the flux is positive. The red arrows point to the sinks. [Color figure can be viewed in the online issue, which is available at www.interscience.wiley.com.]

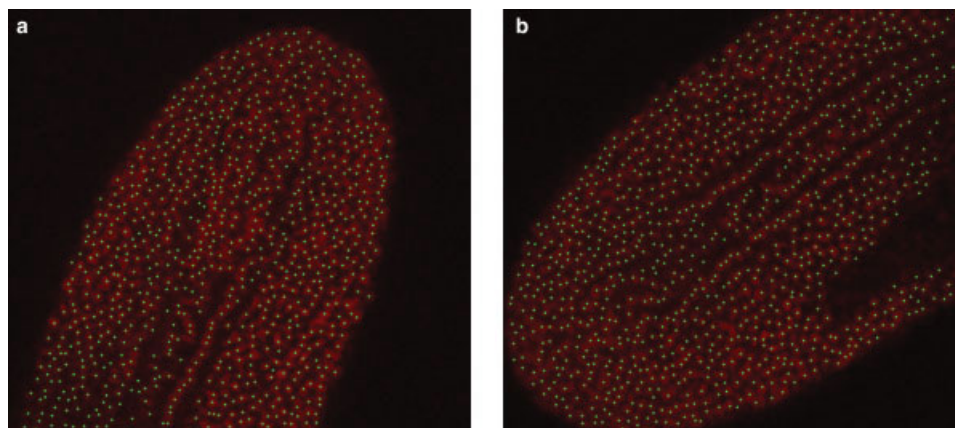


Figure 9. (a) and (b) are two examples of detection of nuclei in zebrafish presomitic mesoderm. The green points indicate the centers of detected nuclei. [Color figure can be viewed in the online issue, which is available at www.interscience.wiley.com.]

maximum false negative rate and maximum false positive rate are 2.8 and 0.3%, respectively. Table 1 shows the details. These results demonstrate that the proposed method has good performance in detecting closely juxtaposed nuclei.

Rohon-Beard sensory neuron detection. The zebrafish has been used to study Alzheimer's disease related genes. For example, we have used antisense morpholinos (MOs) to knock down the expression of zebrafish genes *Psen1*, *Aph-1*, or *Pen-2*, essential components of the γ -secretase complex (26). It has been shown that knockdown of *Pen-2* (*Pen-2* MO injection) caused a loss of RB neurons (26). Previously we have shown by manual and computer-assisted quantification (16) that the loss of RB neurons could be rescued by the co-injection of *Pen-2ΔC* RNA. However, the quantification approaches we used in previous studies resulted in a relatively high false positive rate (16). As an accurate quantification of the number of RB neurons in MO-injected zebrafish is necessary to analyze *PEN-2* function, we use new algorithms in this study.

Here we perform automated detection of RB sensory neurons in the spinal cord stained with anti-acetylated tubulin antibody (25) using the computational algorithm outlined

above. The test dataset is from the Xia Lab of Harvard Medical School. The final results of neuron detection for control MO injected fish are exemplified here in Figure 10. Compared with manual counting by experts, the computerized algorithm achieves a false negative rate of 6.4% and a false positive rate of 0% as shown in Figures 10a and 10b (Case 1 in Table 2). In the example shown in Figures 10c and 10d, the computerized algorithm achieves a false negative rate of 3.6% and a false positive rate of 0%. Notably, we employed a mean-shift clustering method in the color space (31) to decrease the false positive rates from 9.6 and 3.6% to 0 and 0%, respectively. For more detailed information about the mean shift clustering, we refer the reader to the work in (32). The detected neuron centers are clustered into different classes based on their color information. The outliers, as represented by the red dots in Figures 10b and 10d, are removed. Figures 10e and 10f show the color space clustering results from Figures 10b and 10d, respectively.

We have applied this method to 30 images of RB neurons. The average false negative rate and false positive rate are 5 and 3%, respectively. The maximum false negative rate and maximum false positive rates are 8.4 and 8.6%, respectively. Table 2 shows the details. These results further demonstrate the good performance of the proposed method in terms of detection sensitivity and specificity.

Table 1. False Negative Rate (FNR) and False Positive Rate (FPR) in Nuclei Detection

CASE	FNR (%)	FPR (%)
1	1.10	0.20
2	2.60	0.30
3	2.10	0.10
4	1.50	0.10
5	1.80	0.20
6	1.80	0.20
7	2.80	0.10
8	2.50	0.20
9	2.50	0.10
10	1.70	0.20

The maximum FNR and maximum FPR are 2.8 and 0.3, respectively. And the average FNR and average FPR are 2.0 and 0.2, respectively.

Retina cell detection. Zebrafish is an attractive model to study retinal neurogenesis (3–5). Counting the number of neurons, such as ganglion cells, amacrine cells, and photoreceptors, is crucial for studying retina development in wild-type and mutant zebrafish (1,2). Laborious counting of cells in wild-type and mutant retinæ is frequently required while studying gene function in the developing eye (1,15,33).

We have applied the automated detection algorithm outlined above to count retinal cells in zebrafish. The dataset used in these tests were provided by the Malicki Lab at Harvard Medical School. Figure 11a shows an example of a retinal section stained with the DNA-binding dye Yo-Pro (3,5). The number of nuclei detected is used to evaluate the number of cells. The detection result is overlaid on the original image. It is apparent that most cell nuclei in the retina are accurately detected, even though many of them are touching each other.

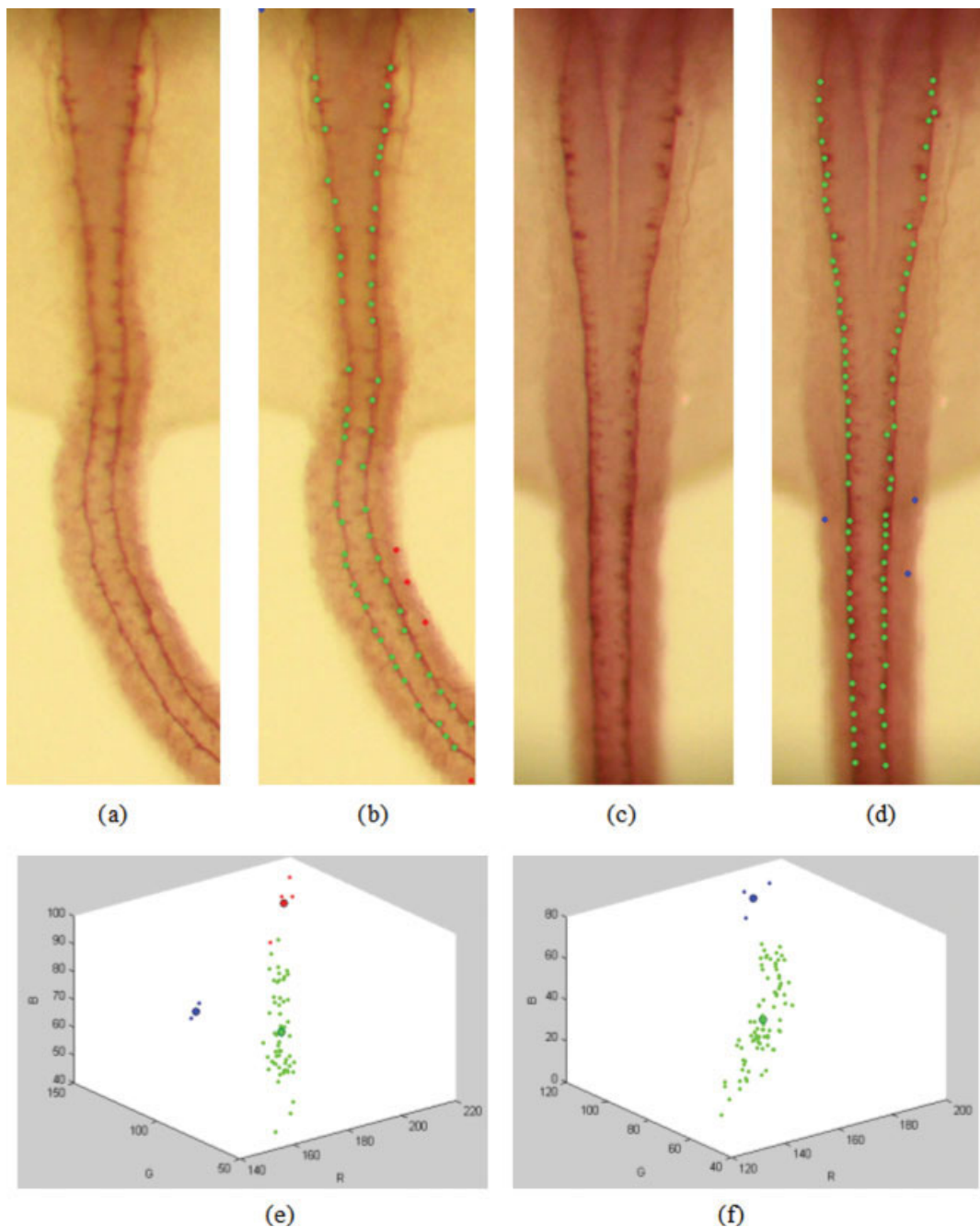


Figure 10. Detection of RB neurons. (a) and (c): original images. (b) and (d): automated detection results. (e) and (f): mean shift clustering results in color space. The red dots and blue dots are outliers and the green dots are detected neurons. [Color figure can be viewed in the online issue, which is available at www.interscience.wiley.com.]

In this case, the average false negative and false positive rates are 2.5 and 2.2%, respectively, compared with expert manual counting.

We have applied this method to 20 images of retinal sections. Overall, the average false negative and false positive rates are 3.7 and 3.1%, respectively. The maximum false negative rate and maximum false positive rate are 6.3 and 5.5%, respectively.

The details are provided in Table 3. The results in this analysis support the conclusion that the proposed method performs well in blob object detection.

DISCUSSION AND CONCLUSION

Currently, the proposed algorithm has been applied to 2D zebrafish images. However, the method could be extended

Table 2. FNR and FPR in RB Neuron Detection

CASE	FNR (%)	FPR (%)
1	6.40	0
2	3.40	0
3	4.30	8.60
4	2.30	0
5	4.10	2.10
6	3.70	4.60
7	2.10	2.30
8	5.20	3.30
9	6.20	4.50
10	4.10	1.60
11	4.30	1.20
12	5.30	3.20
13	6.40	4.20
14	2.10	2.80
15	4.20	0
16	7.10	3.20
17	5.00	3.00
18	7.20	3.10
19	6.40	2.20
20	4.20	6.40
21	3.50	3.30
22	5.40	0
23	4.40	4.30
24	5.20	2.80
25	8.40	2.70
26	5.50	3.30
27	6.20	2.20
28	7.10	3.10
29	7.20	5.20
30	3.00	2.20

The maximum FNR and maximum FPR are 8.4 and 8.6, respectively. And the average FNR and average FPR rate are 5 and 3, respectively.

to 3D images. The difference is that the vector fields have three components in 3D images, and that the flux computing, thresholding and nonmax suppression will be performed in 3D space. The method has several advantages over previous approaches. Firstly, it is able to detect densely spaced or connected blob objects robustly, and no sophisticated rules are used. Secondly, the method could be applied in many different situations. The assumption of this method is that the centers of blobs objects are brighter or darker than nearby regions. Thirdly, the framework of the method is flexible and could be easily extended to 3D images. The disadvantage of the proposed method is that it may display difficulties while processing the images of textured blob objects.

In summary, we have presented a robust method for the detection of blob objects. Validation studies using synthesized images and experimental zebrafish images from three research laboratories have shown that this method is characterized by a good, consistent performance in blob object detection while using different kinds of 2D zebrafish images. In particular, the

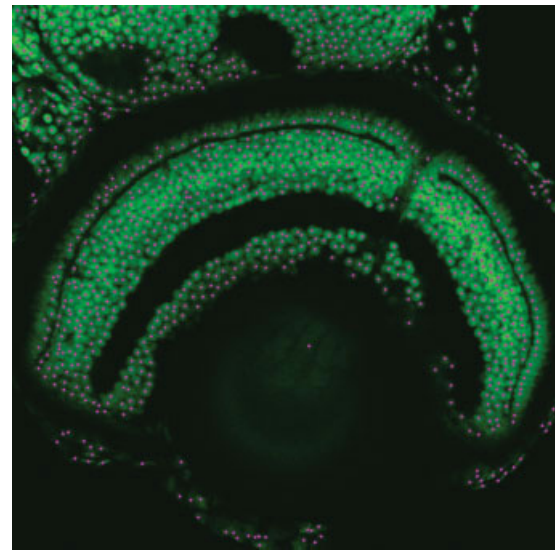


Figure 11. Transverse cryosections stained with DNA-binding dye, Yo-Pro. Quantitative analysis of retinal cells. The pink points indicate the centers of detected cells. [Color figure can be viewed in the online issue, which is available at www.interscience.wiley.com.]

proposed method is able to differentiate closely juxtaposed or connected blob objects with high specificity and efficiency in different situations. We have integrated this method into our ZFIQ (Zebrafish Image Quantitator) platform, and will make it available to the zebrafish research community.

Table 3. FNR and FPR in Retina Cell Detection

CASE	FNR (%)	FPR (%)
1	2.5	2.2
2	2.3	2.2
3	3.3	3.4
4	2.5	0.3
5	3.5	2.3
6	4.4	4
7	2.7	2.2
8	2.7	5.2
9	4.3	2.3
10	2.5	2.2
11	3.4	2.7
12	4.4	5.5
13	4.2	3.2
14	3.3	4.2
15	2.2	2.1
16	6.3	2.5
17	4.5	3.1
18	5.2	3.7
19	5.5	4.3
20	5.1	4.5

The maximum FNR and maximum FPR are 6.3 and 5.5, respectively. And the average FNR and average FPR rate are 3.7 and 3.1, respectively.

LITERATURE CITED

- Pujic Z, Omori Y, Tsujikawa M, Thisse B, Thisse C, Malicki J. Reverse genetic analysis of neurogenesis in the zebrafish retina. *Dev Biol* 2006;293:330–347.
- Tsujikawa M, Malicki J. Intraflagellar transport genes are essential for differentiation and survival of vertebrate sensory neurons. *Neuron* 2004;42:703–716.
- Malicki J. Harnessing the power of forward genetics - analysis of neuronal diversity and patterning in the zebrafish retina. *Trends Neurosci* 2000;23:531–541.
- Baier H, Klostermann S, Trowe T, Karlstrom RO, Nusslein-Volhard C, Bonhoeffer F. Genetic dissection of the retinotectal projection. *Development* 1996;123:415–425.
- Malicki J, Neuhauss SC, Schier AF, Solnica-Krezel L, Stemple DL, Stainier DY, Abdelilah S, Zwartkruis F, Rangini Z, Driever W. Mutations affecting development of the zebrafish retina. *Development* 1996;123:263–273.
- Haffter P, Granato M, Brand M, Mullins MC, Hammerschmidt M, Kane DA, Odenthal J, van Eeden FJM, Jiang YJ, Heisenberg CP, Kelsh RN, Furutani-Seiki M, Vogelsang E, Beuchle D, Schach U, Fabian C, Nusslein-Volhard C. The identification of genes with unique and essential functions in the development of the zebrafish. *Danio rerio*. *Development* 1996;123:1–36.
- Holley SA, Geisler R, Nusslein-Volhard C. Control of her1 expression during zebrafish somitogenesis by a delta-dependent oscillator and an independent wavefront activity. *Genes Dev* 2000;14:1678–1690.
- Julich D, Hwee Lim C, Round J, Nicolajae C, Schroeder J, Davies A, Geisler R, Lewis J, Jiang YJ, Holley SA. beamter/deltaC and the role of Notch ligands in the zebrafish somite segmentation, hindbrain neurogenesis and hypochord differentiation. *Dev Biol* 2005;286:391–404.
- Streisinger G, Walker C, Dower N, Knauber D, Singer F. Production of clones of homozygous diploid zebra fish (*Brachydanio rerio*). *Nature* 1981;291:293–296.
- Patton EE, Zon LI. The art and design of genetic screens: Zebrafish. *Nat Rev Genet* 2001;2:956–66.
- Stern HM, Zon LI. Cancer genetics and drug discovery in the zebrafish. *Nat Rev Cancer* 2003;3:533–539.
- Penberthy WT, Shafizadeh E, Lin S. The zebrafish as a model for human disease. *Front Biosci* 2002;7:d1439–1453.
- Benali A, Leefken I, Eysel U, Weiler E. A computerized image analysis system for quantitative analysis of cells in histological brain sections. *J Neurosci Methods* 2003;125:33–43.
- Klimaschewski L, Nindl W, Pimpl M, Waltinger P, Pfaller K. Biolistic transfection and morphological analysis of cultured sympathetic neurons. *J Neurosci Methods* 2002;113:63–71.
- Doerre G, Malicki J. A mutation of early photoreceptor development, mikre oko, reveals cell-cell interactions involved in the survival and differentiation of zebrafish photoreceptors. *J Neurosci* 2001;21:6745–6757.
- Liu T, Lu J, Wang Y, Campbell WA, Huang L, Zhu J, Xia W, Wong ST. Computerized image analysis for quantitative neuronal phenotyping in zebrafish. *J Neurosci Methods* 2006;153:190–202.
- Lindeberg T. Detecting salient blob-like image structures and their scales with a scale-space primal sketch: A method for focus-of-attention. *Int J Comput Vis* 1993;11:238–318.
- Sjostrom P, Frydel B, Wahlberg L. Artificial neural network-aided image analysis system for cell counting. *Cytometry* 1999;36:18–26.
- Chen X, Zhou X, Wong ST. Automated segmentation, classification, and tracking of cancer cell nuclei in time-lapse microscopy. *IEEE Trans Biomed Eng* 2006;53:762–766.
- Shain W, Kayali S, Szarowski D, Davis-Cix M, Ancin H, Bhattacharjya AK, Roysam B, Turner JN. Application and quantitative validation of computer-automated three-dimensional counting of cell nuclei. *Microsc Microanal* 1999;5:106–119.
- Lin G, Adiga U, Olson K, Guzowski J, Barnes C, Roysam B. A hybrid 3D watershed algorithm incorporating gradient cues and object models for automatic segmentation of nuclei in confocal image stacks. *Cytometry Part A* 2003;56A:23–36.
- Yang Q, Parvin B. Harmonic cut and regularized centroid transform for localization of subcellular structures. *IEEE Trans Biomed Eng* 2003;50:469–475.
- Yang Q, Parvin B. Perceptual organization of radial symmetries. In: *IEEE Computer Society Conference on Computer Vision and Pattern Recognition*. Washington, DC: IEEE; 2004. pp 320–325.
- Byun J, Vu N, Bsumengen B, Manjunath B. Quantitative analysis of immunofluorescent retinal images. *IEEE International Symposium on Biomedical Imaging*. Washington, DC: IEEE; 2006. pp 1268–1271.
- Kort EJ, Jones A, Daumbach M, Hudson EA, Buckner B, Resau JH. Quantifying cell scattering: The blob algorithm revisited. *Cytometry Part A* 2003;51A:119–126.
- Campbell WA, Yang H, Zetterberg H, Baulac S, Sears JA, Liu T, Wong ST, Zhong TP, Xia W. Zebrafish lacking Alzheimer presenilin enhancer 2 (Pen-2) demonstrate excessive p53-dependent apoptosis and neuronal loss. *J Neurochem* 2006;96:1423–1440.
- Xu C, Prince J. Snakes, shapes, and gradient vector flow. *IEEE Trans Image Process* 1998;7:359–369.
- Davatzikos C, Prince J, Bryan R. Image registration based on boundary mapping. *IEEE Trans Med Imaging* 1996;15:112–115.
- Bajcsy R, Kovacic S. Multiresolution elastic matching. *Comput Vis Graphic Image Process* 1989;46:1–21.
- Siddiqi K, Bouix S, Tannenbaum A, Zucker S. The Hamilton-Jacobi skeleton. *IEEE International Conference on Computer Vision*. Kerkyra: IEEE; 1999. pp 828–834.
- Mara A, Schroeder J, Chalouni C, Holley SA. Priming, initiation and synchronization of the segmentation clock by deltaD and deltaC. *Nat Cell Biol* 2007;9:523–530.
- Comaniciu D, Meer P. Mean shift: A robust approach toward feature space analysis. *IEEE Trans Pattern Anal Mach Intell* 2002;24:603–619.
- Avanesov A, Dahm R, Sewell WF, Malicki JJ. Mutations that affect the survival of selected amacrine cell subpopulations define a new class of genetic defects in the vertebrate retina. *Dev Biol* 2005;285:138–155.